ELSEVIER

Contents lists available at ScienceDirect

Journal of Solid State Chemistry

journal homepage: www.elsevier.com/locate/jssc



Synthesis, crystal structure, and magnetic properties of a one-dimensional chain antiferromagnet $NiC_2O_4 \cdot 2NH_3$



Fenghua Ding ^a, Kent J. Griffith ^a, Chi Zhang ^a, Jing Zhan ^{b,***}, Hongcheng Lu ^{c,**}, Kenneth R. Poeppelmeier ^{a,*}

- ^a Department of Chemistry, Northwestern University, Evanston, IL, 60208, USA
- ^b School of Metallurgy and Environment, Central South University, Changsha, Hunan, 410083, China
- ^c School of Chemistry and Chemical Engineering, Huazhong University of Science and Technology, Wuhan, 430074, China

ARTICLE INFO

Keywords: Exploratory synthesis Crystal structures Solid-state NMR Antiferromagnetic One-dimensional chain

ABSTRACT

NiC₂O₄·2NH₃ was synthesized hydrothermally, and its structure was solved by single-crystal X-ray diffraction. Accordingly, NiC₂O₄·2NH₃ crystallizes in the centrosymmetric monoclinic space group C2/m (no. 12) with lattice parameters of a=10.767(5) Å, b=5.414(2) Å, c=5.005(2) Å and $\beta=96.3(4)^\circ$. The NiO₄N₂ octahedra align in a parallel pattern through shared $C_2O_4^{2-}$ units and thus form linear one-dimensional (1D) chains extending along the b-axis. These linear chains are separated along the a-axis by NH₃ molecules and weakly coupled with each other through hydrogen bonding. 1 H and 13 C solid-state NMR revealed isotropic resonances at -115(3) ppm and -312(5) ppm, respectively, for NiC₂O₄·2NH₃, the ammonia protons and oxalate carbons being paramagnetically shifted via the Fermi contact interaction from d^8 Ni(II). Room-temperature paramagnetic shift anisotropies of 400(30) ppm for 1 H and 780(40) ppm for 13 C were determined from simulations of the spinning sideband manifolds. Magnetic susceptibility shows a broad maximum around $T(\chi_{max}) = 35$ K, suggesting well-developed spin–spin correlations along the Ni–C₂O₄–Ni chains. No long-range order is observed down to 2 K, which is further confirmed by heat capacity results. The intrachain interaction J/k of -31.0 K is estimated by fitting the data with a 1D spin chain model. The isothermal magnetization curve at 2 K shows a field-induced phase transition around 5 T. The magnetization value at 9 T is only 0.087 μ_B , which is far from saturation. All magnetic results indicate NiC₂O₄-2NH₃ is a good 1D chain quantum antiferromagnet.

1. Introduction

Low-dimensional magnetic compounds, especially single-molecule magnets (SMMs) and one-dimensional (1D) single-chain magnets (SCMs), show unique magnetic properties that originate from their quantum character [1–3]. These properties lead to applications including single-chain magnets for data storage and quantum spintronic devices [4]. Slow magnetic relaxation is the key property for both SMMs and SCMs. The occurrence of slow relaxation and Arrhenius behavior of the relaxation time in such systems was predicted using a one-dimensional Ising model [5]. Generally, slow magnetic relaxation results from large spin values of the ground state and/or strong uniaxial magnetic anisotropy in SCMs. To realize and design SCM systems, two essential aspects should be considered. First, because an ideal 1D single-chain system is

impossible to realize in the solid-state, quasi-1D crystal structures with spin chains that are well separated by nonmagnetic atoms are desired. Second, the spin carriers must exhibit strong uniaxial magnetic anisotropy in order to have low-dimensional magnetism (*i.e.*, without three-dimensional ordering). Therefore, a stronger intra-chain coupling with a weaker inter-chain magnetic interaction is needed [6–9]. These requirements are different from those of three-dimensional magnetism [10–12].

The most explored magnetic systems contain the late first-row transition metals, e.g., $\mathrm{Fe^{3+}}$, $\mathrm{Co^{2+}}$, $\mathrm{Ni^{2+}}$ and $\mathrm{Cu^{2+}}$, due to their variable spin lattices and tunable coupling types, such as transitions between ferromagnetism and antiferromagnetism [6,13–16]. Coordination chemistry and the variety of available molecular building blocks enable the design of new crystalline solids with 1D structures. Among these building

E-mail addresses: zhanjing@csu.edu.cn (J. Zhan), hcl@hust.edu.cn (H. Lu), krp@northwestern.edu (K.R. Poeppelmeier).

^{*} Corresponding author.

 $[\]ast\ast$ Corresponding author.

^{***} Corresponding author.

blocks, rigid ligands with low symmetry, such as oxalate, $C_2O_4^{2-}$, have been used to obtain 1D linear or zigzag arrangements [17-22]. In order to interfere with the potential coupling of the 1D chains to form 2D or 3D structures, $d^{10}s^2$ lone pair ions (e.g., I^{5+} , Se^{4+} , Te^{4+} , As^{3+}) or halide anions have been introduced as spacer units [23,24]. Following this strategy, the zigzag chain compound Bi₂Fe(SeO₃)₂OCl₃ [23] and sawtooth chain compound Rb₂Fe₂O(AsO₄)₂ [25] were reported, and their magnetic properties were characterized. Analogously, ammonia with a lone pair (in, e.g., mer-[FeF3(NH3)3]) [26] is believed to act as a terminal ligand rather than a bridging ligand in late transition metal octahedral complexes [27-29]. The choice of ligand not only tunes the structural dimensionality but also alters the energetics based on the metal-ligand bond strength [30], influencing the magnetic properties. Further, from the crystal field perspective, strong-field ligands favor low-spin electron configurations while weak-field ligands lead to high-spin configurations. The magnetic properties of complexes containing co-ligands may also be influenced by packing differences, even in the absence of electron configuration differences. For instance, the compounds [Co(N- $CS_{2}(bpa)_{n}$ and $[Co(NCS)_{2}(bpe)]_{n}(bpa = 1,2-bis(4-pyridyl)-ethane; bpe$ = 1,2-bis(4-pyridyl)-ethylene) differ in their interchain interactions [31]. The magnetic properties and the anisotropy at the metal center in $[Co(NCS)_2(L)_2]_n$ (L = aniline, morpholine, and ethylenethiourea) are influenced by changes in L [32]. Interesting magnetic properties and insights can be expected from new co-ligand complexes.

Following this line of reasoning, we chose oxalate and ammonia as coligands with the aim of obtaining 1D structural compounds. A new 1D chain magnetic compound NiC₂O₄·2NH₃ was successfully synthesized with a hydrothermal approach. Magnetic susceptibility shows a broad maximum around 35 K while no long-range order is observed down to 2 K. Field-dependent magnetization at 2 K shows a field-induced transition around 5 T. Magnetic results indicate NiC₂O₄·2NH₃ exhibits well-behaved 1D magnetism. Herein, we report the structure and magnetic properties of this new compound. Single-crystal X-ray diffraction and $^1\mathrm{H}$ and $^{13}\mathrm{C}$ solid-state nuclear magnetic resonance are consistent with the model of NH₃ as a ligand directly bound to the nickel(II) center with bridging oxalate ligands.

2. Experimental procedures

2.1. Synthesis

NiC2O4·2NH3 was synthesized in two steps. First, 6.0 mmol of NiCl₂·6H₂O (1.428 g, 99.0%, Sigma-Aldrich), 8.4 mmol of H₂C₂O₄ (0.756 g, 99.0%, Sigma-Aldrich), and 4.0 mL ammonium hydroxide solution (NH₃·H₂O, 28.0% by weight, Sigma-Aldrich) were reacted under hydrothermal conditions in a 125 ml Teflon-lined Parr pressure vessel filled with 20 ml of deionized H2O as backfill. Pressure vessels were heated to 453 K for 48 h, followed by cooling to room temperature at a rate of 0.1 K/min. The Teflon-lined Parr autoclave was then left undisturbed at room temperature for another 12 h to allow crystallization. Crystals of NiC2O4·2NH3 were then recovered via vacuum filtration and vacuum drying with a yield of about 85 mol% based on nickel. A milder solution method at ambient pressure, 333 K, and 2 h reaction time was also explored to synthesize the title compound. The target phase was not found (see Fig. 1). Hydrothermal conditions may be critical for the synthesis of NiC₂O₄·2NH₃. The target phase plus an unknown secondary phase were observed (Fig. 1) after the first-round of hydrothermal reaction. Therefore, purification and recrystallization were needed. Typically, one more cycle of hydrothermal reaction was performed. The initial products and an additional 3 mL ammonium hydroxide solution were added to a 125 ml Teflon-lined Parr pressure vessel filled with 20 ml of deionized H₂O as backfill. The same heating procedure was applied. The simulated powder X-ray diffraction pattern was obtained using the software Mercury [33].

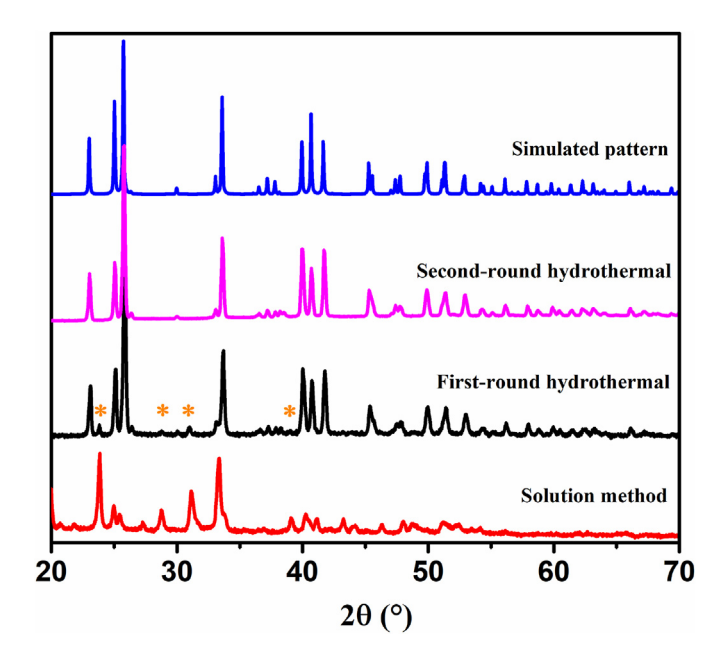


Fig. 1. Simulated and experimental X-ray powder diffraction patterns for $NiC_2O_4 \cdot 2NH_3$. The unknown secondary phase is denoted with orange stars.

2.2. Crystal structural characterization

A blue, transparent, blocky crystal was chosen for structure determination. Single-crystal XRD data were collected at 100 K with a Rigaku Oxford XtaLAB Synergy-DW diffractometer equipped with monochromatic Mo $K\alpha$ radiation ($\lambda=0.71073$ Å). The crystal-to-detector distances were set to 50 mm. The CrysAlisPro software was used for data reduction and integration [34]. The structures were established by the direct method and refined through the full-matrix least-squares fitting on F^2 using OLEX2 [35]. All atoms were refined using full-matrix least-squares techniques, and final least-squares refinement was on F_0^2 with data having $F_0^2 \geq 2\sigma(F_0^2)$. Numerical absorption corrections were carried out using the SCALE program for an area detector. The structures were solved using Shel-XT to determine the atomic coordinates of the cations. The structures were examined for possible missing symmetry elements with PLATON, and no additional symmetry was found [36]. Other crystallographic data are reported in the CIF.

2.3. Phase identification

Powder XRD measurements were performed at room temperature on a Rigaku Ultima diffractometer with graphite monochromatized Cu $K\alpha$ ($\lambda=1.5418$ Å) radiation. The measured powder XRD pattern of NiC₂. O₄·2NH₃ matches the simulated pattern from the single-crystal X-ray diffraction structure solution (Fig. 1).

2.4. Solid-state nuclear magnetic resonance spectroscopy

NMR spectra of polycrystalline $NiC_2O_4\cdot 2NH_3$ were measured at 9.4 T with a Bruker Advance III spectrometer. The powder sample was packed into a zirconia rotor. Paramagnetic spectra were recorded at multiple offset frequencies to overcome the limited excitation bandwidth and measure accurate maximum intensities over the wide anisotropic line shapes. Variable off-set spectra are overlaid, the maximum intensity of each sideband tracing out the skyline projection of the line shape expected without excitation bandwidth limitations. Identification of the isotropic chemical shifts was determined by recording spectra at different MAS rates. Frictional heating at 12 kHz (4 mm), 25 kHz (1.9 mm), and 40 kHz

(1.9 mm) MAS is estimated to lead to sample temperatures in this work of 305 K, 304 K, and 317 K, respectively, based on the temperature-dependent ^{207}Pb chemical shift of lead nitrate [37,38]. Adamantane was used as an external secondary chemical shift reference by calibrating its single isotropic ^{1}H resonance to 1.8 ppm and its high-frequency (methylene) ^{13}C resonance to 38 ppm.

 1 H solid-state NMR spectra were recorded with a 1.9 mm Phoenix HFX probe under magic-angle spinning (MAS) at 25–40 kHz with a rotor-synchronized Hahn-echo pulse sequence ($\pi/2$ – τ – π – τ –acquire) and a $\pi/2$ rf pulse of 1.8 μ s (139 kHz). The recycle delay was set to 100 ms and 64 scans were summed for each sub-spectrum. Longer delay times were measured to check for additional resonances from diamagnetic impurities; none were observed.

 ^{13}C solid-state NMR spectra were measured with a 4.0 mm Bruker HX probe at 12–14 kHz MAS. A Hahn-echo was also used for ^{13}C measurements with a $\pi/2$ rf pulse was 2.5 μs (100 kHz). The recycle delay was 50 ms and 32,768 scans were summed for each sub-spectrum. Longer delay times were measured to check for additional resonances from diamagnetic impurities; none were observed.

Simulation of the anisotropic line shapes in the Solid Lineshape Analysis (SOLA) program in TopSpin 4.0.9 enabled the extraction of the full shift tensor quantities ($\delta_{\rm iso}$, $\delta_{\rm SA}$, $\eta_{\rm SA}$). Estimated errors in the reported isotropic shifts (from temperature effects) and anisotropy parameters (from fitting) are given in parentheses. In this study, the Haeberlen convention is used to describe the shift tensor with the isotropic shift $\delta_{\rm iso} = \frac{\delta_{11} + \delta_{22} + \delta_{33}}{3}$; shift anisotropy $\delta_{\rm SA} = \delta_{33} - \delta_{\rm iso}$; and shift asymmetry $\eta_{\rm SA} = \frac{\delta_{22} - \delta_{13}}{\delta_{33} - \delta_{\rm iso}}$. In this definition, the principal components of the shift tensor are ordered such that $|\delta_{33} - \delta_{\rm iso}| \geq |\delta_{11} - \delta_{\rm iso}| \geq |\delta_{22} - \delta_{\rm iso}|$.

2.5. Magnetic properties characterization

A Quantum Design Dynacool Physical Property Measurement System (PPMS) was used to measure the magnetic properties and heat capacity. Heat capacity was measured using a standard relaxation method. A small part of the pelleted disk was employed for this measurement. The pellet was glued onto the calorimetric platform with a small amount of grease. Heat capacity measurements were carried out from 2 to 100 K and with applied magnetic fields of 0 T and 9 T. The contribution of the addenda (platform + grease) was subtracted from the gross data. All measurements used polycrystalline $\rm NiC_2O_4 \cdot 2NH_3$.

3. Results and discussion

3.1. Crystal structure of NiC₂O₄·2NH₃

NiC₂O₄·2NH₃ crystallizes in the centrosymmetric monoclinic space group C2/m. The crystal data are summarized in Table 1 and Tables S1–S3. The asymmetric unit contains one nickel atom, one oxygen atom, one carbon atom, one nitrogen atom and two hydrogen atoms. The local coordination of the nickel octahedra is shown in Fig. 2a. Two symmetry-equivalent nitrogen atoms are located at trans positions along the axial direction, while four oxygen atoms sit at equatorial positions. We observe that the Ni-octahedron is of C_{2h} symmetry with a slightly compressed axial Ni-N distance of 2.080(14) Å. The four equatorial Ni-O distances are 2.086(8) Å. The O-Ni-O angle is 80.5(6)° because the two O atoms are from the same $C_2O_4^{2-}$ unit and are thus restricted. The octahedral units align in a parallel pattern by sharing the C₂O₄²⁻ unit between two NiO₄N₂ octahedra. This parallel alignment leads to the structure featuring linear chains running along the b-axis (see Fig. 2b), among which adjacent chains align with each other through hydrogen bonds (2.525(7) Å). The rectangular prismatic morphology can be seen in Fig. S1. The bond valence sums for NiC₂O₄·2NH₃ are calculated using the formula: $V_i = \sum_{j} S_{ij} = \sum_{j} exp\left\{\frac{(r_0 - r_{ij})}{B}\right\}$, where S_{ij} is the bond valence associated with bond length r_{ij} and r_0 and B (usually 0.37) are empirically

Table 1 Crystal data and structure refinement metrics for $NiC_2O_4 \cdot 2NH_3$.

Empirical formula	$NiC_2O_4N_2H_6$
Temperature /K	100
Crystal System	monoclinic
Space Group	C2/m
a /Å	10.767(5)
b /Å	5.414(2)
c /Å	5.005(2)
β /°	96.3(4)
Volume /Å ³	290.0(2)
Z	2
$\rho_{\rm calc}$ /g·cm ⁻³	2.070
μ / mm^{-1}	3.287
F (000)	184.0
Crystal size /mm ³	$0.04\times0.07\times0.18$
Radiation	Mo $K\alpha$ ($\lambda = 0.71073 \text{ Å}$)
2θ range for data collection /°	7.616 to 67.652
Reflections collected	5088
Independent reflections	593 [R_{int} =0.030, R_{sigma} =0.016]
Goodness-of-fit on F^2	1.042
Final R indexes [all data]	$R_1 = 0.0205, wR_2 = 0.0524$
Largest diff. peak/hole /e·Å ⁻³	0.759/-0.877

determined parameters [39]. The results of bond valence sum calculations are 2.06 and 1.77 for the Ni and O atoms, which indicates that they are in the expected oxidation states of +2 and -2, respectively.

 1 H and $^{1ar{3}}$ C paramagnetic solid-state MAS NMR measurements were conducted in order to further examine the structural model. A ¹H isotropic resonance was observed at -115(3) ppm amongst a large manifold of spinning sidebands (Fig. 3). The asymmetric experimental lineshape is consistent with incompletely averaged coupling to the quadrupolar ¹⁴N nucleus [40,41]. The large negative shift, rapid relaxation, and large paramagnetic shift anisotropy are consistent with ammonia directly bound to a Ni(II) center. Simulations of the spinning sideband manifold revealed a shift anisotropy (δ_{SA}) of 400(30) ppm with an asymmetry (η_{SA}) of 0.55(10). Rouf et al. studied the related molecular solid trans-[Ni(acac)2(NH3)2] as a model system to evaluate paramagnetic NMR interactions and first-principles methods [42]. In that work, the ¹H signal from the Ni(II)–NH₃ was broadened beyond detection at 20 kHz MAS and 11.7 T; however, a 2H spectrum of the deuterated analogue trans-[Ni(acac)2(ND3)2] revealed an ND3 shift of -113 ppm, virtually identical to the ¹H shift of NiC₂O₄·2NH₃ observed here [42]. Quantum chemical calculations from Rouf et al. indicated that the major contributions for the isotropic Ni(II)-N(H/D)3 shift are the conventional chemical shift (i.e., orbital shift) and the Fermi contact shift [42]. The orbital contribution to the overall shift was essentially the same as for diamagnetic NH3; and, amongst the various paramagnetic NMR interactions, the Fermi contact contribution to the shift was dominated by the non-relativistic contact term.

 13 C MAS NMR (Fig. 4) exhibited a similarly broad powder pattern with an isotropic resonance at -312(5) ppm, a shift anisotropy of

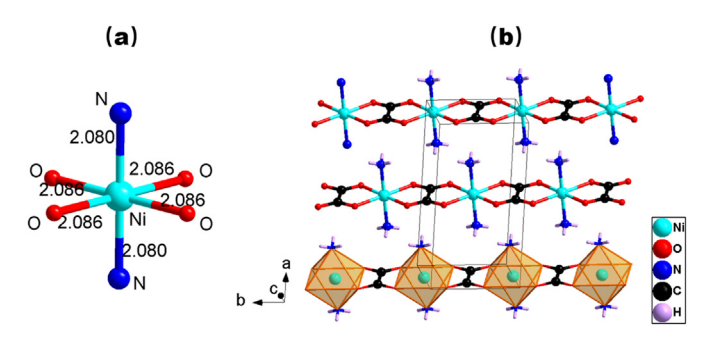


Fig. 2. (a) The local octahedral environment of Ni, with bond lengths in units of angstrom. (b) Ball-and-stick and polyhedral representations of the structure of NiC₂O₄·2NH₃.

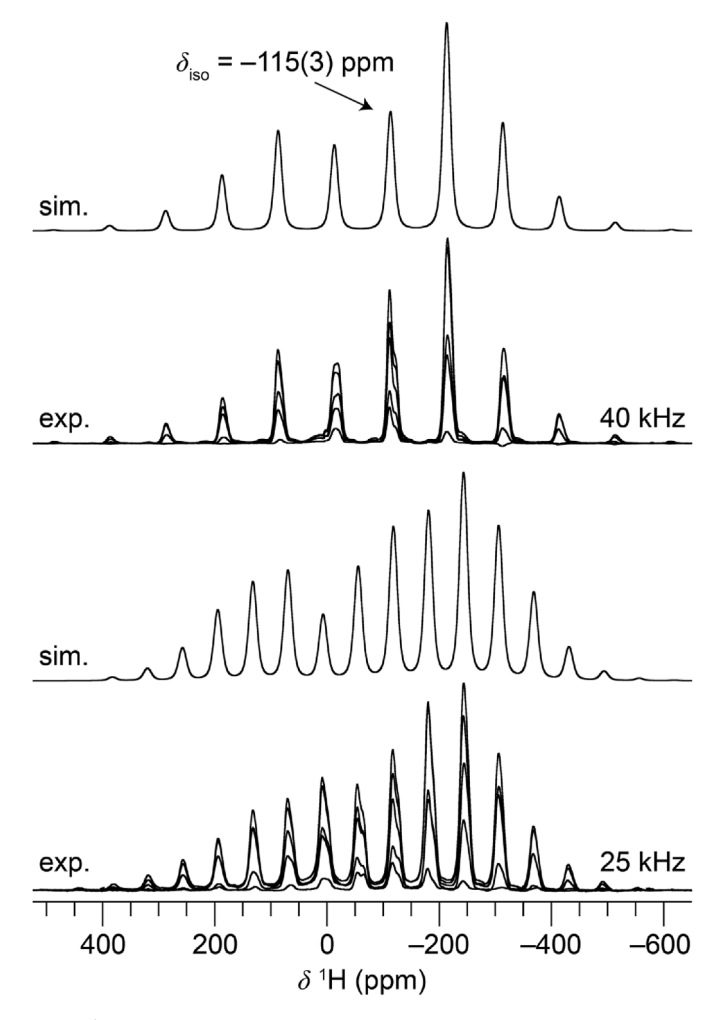


Fig. 3. 1 H MAS NMR echo spectra of NiC₂O₄·2NH₃. Overlaid frequency-stepped experimental spectra are shown below the simulation of the skyline projection at 40 kHz (top two panels) and 25 kHz (bottom two panels). Note that the highest signal is not the position of the isotropic shift owing to the large shift anisotropy.

780(40) ppm, and an asymmetry of 0.73(5). To the best of our knowledge, this is the first 13 C NMR report of the oxalate ligand bound to Ni(II). The acetylacetonate is structurally related; however, the 13 C=O shift in [Ni(II)(acac)₂(NH₃)₂] was observed at +199(1) ppm and thus the hyperfine interactions clearly differ significantly between oxalate and acac complexes of Ni(II) [42,43].

Overall, the well-defined NMR lineshapes and apparent absence of inhomogeneous broadening are expected from a high-spin octahedral d^8 electron configuration [44]. There is good agreement between the experimental and simulated anisotropic powder lineshapes even neglecting bulk magnetic susceptibility (BMS) effects, which vary between particles and within a single particle [45]. We note that theoretical methods to accurately calculate paramagnetic shift anisotropies have been developed in recent years, and this system may be an interesting model to further develop structure–spectral relationships in paramagnetic NMR utilizing both the isotropic and anisotropic shift components [45,46].

3.2. Magnetic properties of NiC₂O₄·2NH₃

Each Ni²⁺ ion in the structure has a d^8 electron configuration with two unpaired electrons in e_g orbitals. Thus, the temperature-dependent magnetic susceptibility from 2 to 300 K is measured at 0.1 T as shown in Fig. 5. The $\chi(T)$ curve shows a notable feature of low-dimensional

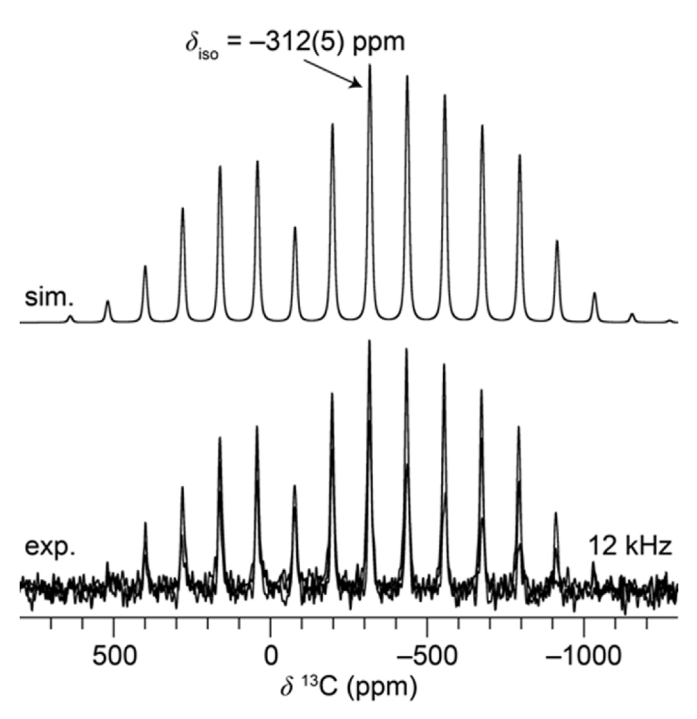


Fig. 4. 13 C MAS NMR echo spectra of NiC₂O₄·2NH₃. Overlaid frequency-stepped experimental spectra are shown below the simulation of the skyline projection.

magnetism with a broad maximum around $T(\chi_{max})=35$ K, which is originated from well-developed spin–spin correlations along the Ni–C₂O₄–Ni chains. This suggests strong intrachain interactions. Meanwhile, no signature of long-range order is seen down to 2 K in the magnetic susceptibility data. A Curie–Weiss fitting between 250 and 300 K is applied, leading to the effective magnetic moment $\mu_{\rm eff}$ of 3.37(3) $\mu_{\rm B}$ and Weiss temperature θ of –76.6(9) K (Fig. S2). The negative Weiss temperature suggests that the dominant interaction in NiC₂O₄·2NH₃ is antiferromagnetic (AFM). The $\mu_{\rm eff}$ value is larger than the spin-only value for a free ion of Ni²⁺, which may be due to unquenched orbital contribution or anisotropy [47,48]. Note that it also cannot be ruled out that the system may not be purely paramagnetic state up to 300 K. Also, upon cooling, the χT starts to decrease even from 300 K, as shown in Fig. S2, confirming that the AFM intrachain interaction is strong.

To estimate the intrachain interaction, the experimental data of magnetic susceptibility between 20 and 300 K is fitted by an S=1 spin chain model as follows (Fig. 5) [49]:

$$\chi = \frac{N\mu_B^2 g^2}{k_B T} \frac{2 + 0.0194X + 0.777X^2}{3 + 4.346X + 3.232X^2 + 5.834X^3}$$

Where $X = |J|/k_BT$; N, μ_B , g, k_B , and T are the Avogadro constant, Bohr magneton, Laude factor, Boltzmann constant, and absolute temperature, respectively. J is the intrachain interaction between adjacent Ni²⁺ ions along the chain. The best fit gives $J/k_B = -31.0(2)$ K and g = 2.04(1).

The temperature dependence of the specific heat between 2 and 100 K is shown in Fig. 6. Consistent with the magnetic susceptibility data, no sign of a transition is observed down to 2 K, which further confirms the absence of long-range order. Isothermal magnetization between -9 and 9 T was also measured at various fields as shown in Fig. 7 and S3. For field-dependent magnetization at 2 K, the magnetization curve at low field increases linearly with increasing field. Around 5 T, the slope abruptly changes and magnetization increases more steeply above 5 T. The magnetization is as small as 0.087 $\mu_{\rm B}$ at 9 T, which is far from saturation. The steeper increase of magnetization suggests the existence of a field-induced phase transition around 5 T. The origin of this magnetic transition together with its magnetic behavior at a lower temperature for

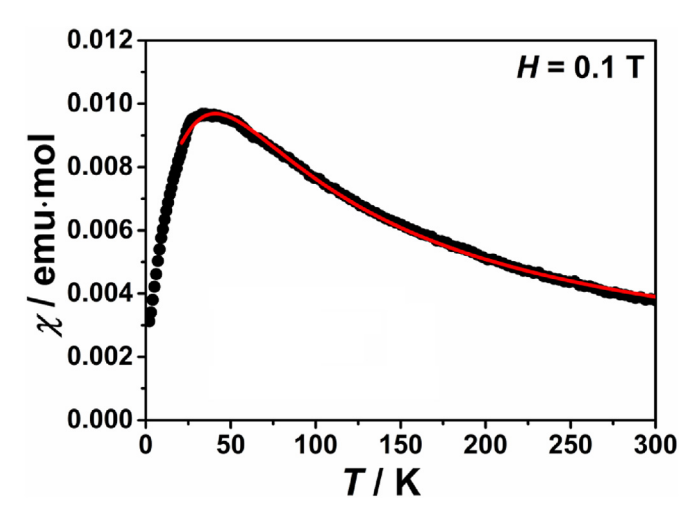


Fig. 5. Temperature-dependence of magnetic susceptibility $\chi(T)$ for NiC₂. O_4 ·2NH₃ measured at 0.1 T (black solid circle). The red solid line is the spin chain fitting between 20 and 300 K.

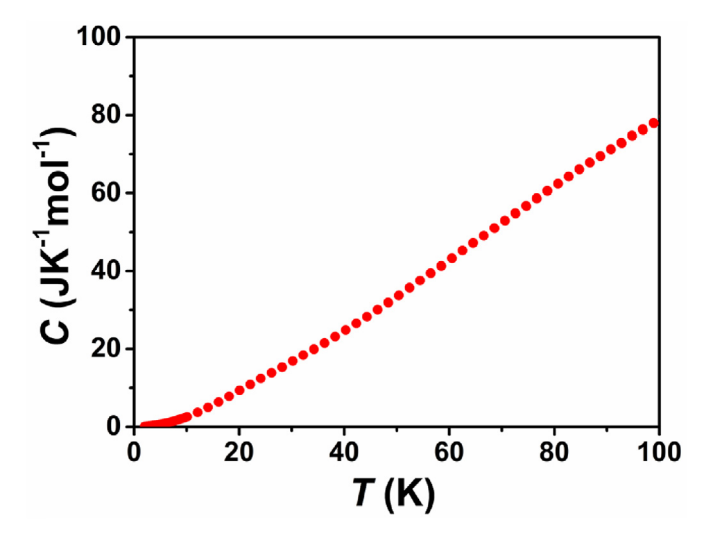


Fig. 6. Specific heat for NiC₂O₄·2NH₃ measured at zero field.

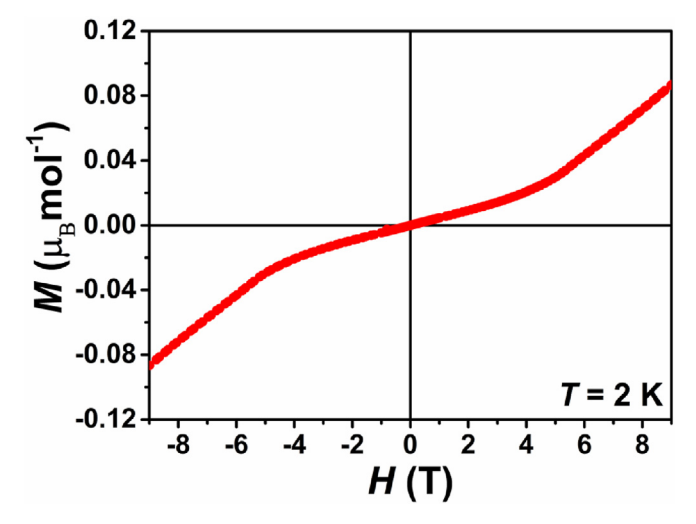


Fig. 7. Isothermal magnetization for NiC₂O₄·2NH₃ measured at 2 K.

 $\text{NiC}_2\text{O}_4\text{·}2\text{NH}_3$ are the topic of a future study with a larger single crystal sample.

4. Conclusion

A new one-dimensional spin-1 antiferromagnetic compound NiC2-O₄·2NH₃ was successfully synthesized and characterized structurally and magnetically. From single-crystal diffraction results, NiC2O4·2NH3 presents as a new type of 1D magnetic chain structure with C₂O₄²⁻ and NH₃ as co-ligands. Two symmetry-equivalent nitrogen atoms are located at trans positions along the axial direction, while four oxygen atoms are located at equatorial positions. The NiO₄N₂ octahedral units align in a parallel pattern through shared C₂O₄²⁻ units and form linear chains running along the b-axis. The adjacent chains are aligned through hydrogen bonds. ¹H and ¹³C solid-state NMR revealed isotropic resonances at -115(3) ppm and -312(5) ppm, respectively, for NiC2-O₄·2NH₃, the ammonia protons and oxalate carbons being paramagnetically shifted via the Fermi contact interaction from *d*⁸ Ni(II). Full anisotropic shift tensors were determined from stepped collection and fitting of the NMR spinning sideband manifolds. Magnetic susceptibility shows a broad maximum around 35 K while no long-range order is observed down to 2 K, which is further confirmed by heat capacity. The isothermal magnetization at 2 K shows a field-induced transition around 5 T. All magnetic results indicate NiC₂O₄·2NH₃ shows a good 1D quantum magnetism. Our results demonstrate that the co-ligand strategy provides a possibility to explore new low-dimensional magnetic compounds.

5. Associated content

Supporting information

X-ray crystallographic file in CIF format; additional magnetic susceptibility data; heat capacities data.

5.1. Accession codes

CCDC 2018052 contains the supplementary crystallographic data for this paper. These data can be obtained free of charge via www.ccdc.cam. ac.uk/data_request/cif, or by emailing data_request@ccdc.cam.ac.uk, or by contacting The Cambridge Crystallographic Data Center, 12 Union Road, Cambridge CB2 1EZ, UK; fax: +44 1223 336033.

CRediT authorship contribution statement

Fenghua Ding: Conceptualization, Writing – original draft, Visualization, Formal analysis, Investigation. Kent J. Griffith: Visualization, Writing – review & editing, Investigation, Formal analysis. Chi Zhang: Formal analysis, Investigation. Jing Zhan: Conceptualization, Writing – original draft, Visualization, Formal analysis, Investigation. Hongcheng Lu: Writing – review & editing. Kenneth R. Poeppelmeier: Supervision, Resources.

Declaration of competing interest

The authors declare that they have no known competing financial interests or personal relationships that could have appeared to influence the work reported in this paper.

Acknowledgements

Dedicated to Professor Alario- Franco on his 80th birthday. This work was supported by funding from the National Science Foundation (DMR-1904701). K.J.G. was supported as part of the Joint Center for Energy Storage Research, an Energy Innovation Hub funded by the U.S. Department of Energy, Office of Science, Basic Energy Sciences. The

single-crystal X-ray and solid-state NMR measurements were acquired at Northwestern University's Integrated Molecular Structure Education and Research Center (IMSERC), which is supported by grants from NSF-NSEC, NSF-MRSEC, the KECK Foundation, the State of Illinois, and Northwestern University. This work made use of the J. B. Cohen X-Ray Diffraction Facility supported by the MRSEC program of the National Science Foundation (DMR-1720139) at the Materials Research Center of Northwestern University. We also thank Professor Weiwei Xie for her helpful comments on the manuscript and magnetic measurements.

Appendix A. Supplementary data

Supplementary data to this article can be found online at https://do i.org/10.1016/j.jssc.2022.123360.

References

- J.S. Miller, M. Drillon, Magnetism: Molecules to Materials IV, vol. 4, John Wiley & Sons, 2001.
- [2] H. Miyasaka, K. Takayama, A. Saitoh, S. Furukawa, M. Yamashita, R. Clérac, Three-dimensional antiferromagnetic order of single-chain magnets: a new approach to design molecule-based magnets, Chem. Eur J. 16 (2010) 3656–3662, https://doi.org/10.1002/chem.200902861.
- [3] N. Hoshino, Y. Sekine, M. Nihei, H. Oshio, Achiral single molecule magnet and chiral single chain magnet, Chem 46 (2010) 6117–6119, https://doi.org/10.1039/ COCC00184H.
- [4] H.L. Sun, Z.M. Wang, S. Gao, Strategies towards single-chain magnets, Coord. Chem. Rev. 254 (2010) 1081–1100, https://doi.org/10.1016/j.ccr.2010.02.010.
- [5] R.J. Glauber, Time-dependent statistics of the Ising model, J. Math. Phys. 4 (1963) 294–307, https://doi.org/10.1063/1.1703954.
- [6] R. Clérac, H. Miyasaka, M. Yamashita, C. Coulon, Evidence for single-chain magnet behavior in a Mn(III)-Ni(II) chain designed with high spin magnetic units: a route to high temperature metastable magnets, J. Am. Chem. Soc. 124 (2002) 12837–12844, https://doi.org/10.1021/ja0203115.
- [7] P.D. Boyd, Q. Li, J.B. Vincent, K. Folting, H.R. Chang, W.E. Streib, J.C. Huffman, G. Christou, D.N. Hendrickson, Potential building blocks for molecular ferromagnets: [Mn₁₂O₁₂(O₂CPh)₁₆(H₂O)₄] with a S=14 ground state, J. Am. Chem. Soc. 110 (1988) 8537–8539, https://doi.org/10.1021/ja00233a036.
- [8] A. Caneschi, D. Gatteschi, R. Sessoli, A.L. Barra, L.C. Brunel, M. Guillot, Alternating current susceptibility, high field magnetization, and millimeter band EPR evidence for a ground S= 10 state in [Mn₁₂O₁₂(Ch₃COO)₁₆(H₂O)₄]-2CH₃COOH·4H₂O, J. Am. Chem. Soc. 113 (1991) 5873–5874, https://doi.org/10.1021/ja00015a057.
- [9] C. Coulon, H. Miyasaka, R. Clérac, Single-chain magnets: theoretical approach and experimental systems, in: Single-molecule Magnets and Related Phenomena, Springer, 2006, pp. 163–206, https://doi.org/10.1007/430_030.
- [10] A. Trukhanov, et al., Crystal structure and magnetic properties of the BaFe $_{12}$. $_x$ Al $_x$ O $_{19}$ (x= 0.1–1.2) solid solutions, J. Magn. Magn Mater. 393 (2015) 253–259, https://doi.org/10.1016/j.jmmm.2015.05.076.
- [11] A. Trukhanov, et al., Control of electromagnetic properties in substituted M-type hexagonal ferrites, J. Alloys Compd. 754 (2018) 247–256, https://doi.org/ 10.1016/j.jallcom.2018.04.150.
- [12] S. Trukhanov, et al., Polarization origin and iron positions in indium doped barium hexaferrites, Ceram. Int. 44 (2018) 290–300, https://doi.org/10.1016/ i.ceramint.2017.09.172.
- [13] R. Becker, M. Prester, H. Berger, P.H. Lin, M. Johnsson, D. Drobac, I. Zivkovic, Crystal structure and magnetic properties of two new cobalt selenite halides: Co₅(SeO₃)₄X₂ (X= Cl, Br), J. Solid State Chem. 180 (2007) 1051–1059, https://doi.org/10.1016/j.jssc.2006.12.035.
- [14] R. Becker, M. Johnsson, R.K. Kremer, P. Lemmens, Crystal structure and magnetic properties of Cu₃(TeO₃)₂Br₂-a layered compound with a new Cu(II) coordination polyhedron, J. Solid State Chem. 178 (2005) 2024–2029, https://doi.org/10.1016/ i.issc.2005.04.011.
- [15] R.F. Takagi, D.T. Hjelmqvist, M. Johnsson, S. Lidin, Helical chains of [MO₅Cl] octahedra-Three compounds in the new family AEM₂Te₃O₈Cl₂ (AE= Ca, Sr and M= Co, Ni), Solid State Sci. 11 (2009) 13–17, https://doi.org/10.1016/j.solidstatesciences.2008.04.009.
- [16] X.T. Liu, X.Y. Wang, W.X. Zhang, P. Cui, S. Gao, Weak ferromagnetism and dynamic magnetic behavior in a single end-to-end azide-bridged nickel(II) chain, Adv. Mater. 18 (2006) 2852–2856, https://doi.org/10.1002/adma.200600253.
- [17] E. Coronado, J.R. Galan-Mascaros, C. Marti-Gastaldo, Single chain magnets based on the oxalate ligand, J. Am. Chem. Soc. 130 (2008) 14987–14989, https:// doi.org/10.1021/ja806298t.
- [18] G.F. Xu, Q.L. Wang, P. Gamez, Y. Ma, R. Clérac, J. Tang, S.P. Yan, P. Cheng, D.Z. Liao, A promising new route towards single-molecule magnets based on the oxalate ligand, Chem 46 (2010) 1506–1508, https://doi.org/10.1039/B920215C.
- [19] E. Coronado, J.R. Galan-Mascaros, C. Marti-Gastaldo, Design of bimetallic magnetic chains based on oxalate complexes: towards single chain magnets, CrystEngComm 11 (2009) 2143–2153, https://doi.org/10.1039/B910490A.

- [20] M.L. Bonnet, C. Aronica, G. Chastanet, G. Pilet, D. Luneau, C. Mathoniere, R. Clérac, V. Robert, Nickel (II) chain with alternating end-on/end-to-end single azido bridges: a combined structural, magnetic, and theoretical study, Inorg. Chem. 47 (2008) 1127–1133, https://doi.org/10.1021/ic702012r.
- [21] M. Hagiwara, N. Narita, I. Yamada, Spin-glass freezing in the S=1 antiferromagnetic Heisenberg chainNiC₂O₄·2[(2-methylimidazole)_x(H₂O)_{1-x}], Phys. Rev. B 55 (1997) 5615, https://doi.org/10.1103/PhysRevB.55.5615.
- [22] J. Renard, M. Verdaguer, L. Regnault, W. Erkelens, J. Rossat-Mignod, J. Ribas, W. Stirling, C. Vettier, Quantum energy gap in two quasi-one-dimensional S=1 Heisenberg antiferromagnets, J. Appl. Phys. 63 (1988) 3538–3542, https://doi.org/ 10.1063/1.340736.
- [23] P.S. Berdonosov, E.S. Kuznetsova, V.A. Dolgikh, A.V. Sobolev, I.A. Presniakov, A.V. Olenev, B. Rahaman, T. Saha-Dasgupta, K.V. Zakharov, E.A. Zvereva, Crystal structure, physical properties, and electronic and magnetic structure of the spin S=5/2 zigzag chain compound Bi₂Fe(SeO₃)₂OCl₃, Inorg. Chem. 53 (2014) 5830–5838, https://doi.org/10.1021/ic500706f.
- [24] J.G. Mao, H.L. Jiang, F. Kong, Structures and properties of functional metal selenites and tellurites, Inorg. Chem. 47 (2008) 8498–8510, https://doi.org/10.1021/ ic8005629.
- [25] V.O. Garlea, L.D. Sanjeewa, M.A. McGuire, P. Kumar, D. Sulejmanovic, J. He, S.-J. Hwu, Complex magnetic behavior of the sawtooth Fe chains in Rb₂Fe₂O(AsO₄)₂, Phys. Rev. B 89 (2014), 014426.
- [26] S.A. Baer, F. Kraus, mer-Triammine Trifluorido Iron(III), mer-[FeF₃(NH₃)₃],
 Z. Naturforsch. B Chem. Sci. 66 (2011) 865–867, https://doi.org/10.1103/ PhysRevB.89.014426.
- [27] T. Schönherr, R. Wiskemannb, D. Mootzb, Crystal structure and ligand field states of [Cr(NH₃)₅NCO](NO₃)₂, Inorg. Chim. Acta. 221 (1994) 93–98, https://doi.org/ 10.1016/0020-1693(94)03960-7.
- [28] C. Sugiura, M. Kitamura, S. Muramatsu, X-ray absorption near-edge structure of complex compounds (NH₄)₃RhCl₆, K₃RuCl₆, and Ru (NH₃)₆Cl₃, J. Chem. Phys. 84 (1986) 4824–4827, https://doi.org/10.1063/1.449970.
- [29] J. Zhan, J.H. Wu, C.F. Zhang, J.F. Yue, Shape-controlled synthesis of novel precursor for preparing fiber-like nickel oxide powders, Min. Metall. Eng. 2 (2010). http://www.kygczz.com/CN/abstract/abstract1457.shtml.
- [30] J. Gao, et al., Mixed metal-organic framework with multiple binding sites for efficient C2H2/CO2 separation, Angew. Chem. Int. Ed. 59 (11) (2020) 4396–4400.
- [31] S. Wöhlert, Z. Tomkowicz, M. Rams, S.G. Ebbinghaus, L. Fink, M.U. Schmidt, C. Näther, Influence of the co-ligand on the magnetic and relaxation properties of layered cobalt (II) thiocyanato coordination polymers, Inorg. Chem. 53 (2014) 8298–8310, https://doi.org/10.1021/ic500572p.
- [32] A. Jochim, T. Lohmiller, M. Rams, M. Böhme, M. Ceglarska, A. Schnegg, W. Plass, C. Näther, Influence of the coligand onto the magnetic anisotropy and the magnetic behavior of one-dimensional coordination polymers, Inorg. Chem. 59 (2020) 8971–8982, https://doi.org/10.1021/acs.inorgchem.0c00815.
- [33] C.F. Macrae, I. Sovago, S.J. Cottrell, P.T. Galek, P. McCabe, E. Pidcock, M. Platings, G.P. Shields, J.S. Stevens, M. Towler, Mercury 4.0: from visualization to analysis, design and prediction, J. Appl. Crystallogr. 53 (2020) 226–235, https://doi.org/ 10.1107/S1600576719014092
- [34] v.A. Saint, Bruker Analytical X-Ray Instruments, Inc., Madison, WI, 2008.
- [35] O.V. Dolomanov, L.J. Bourhis, R.J. Gildea, J.A. Howard, H. Puschmann, OLEX2: a complete structure solution, refinement and analysis program, J. Appl. Crystallogr. 42 (2009) 339–341, https://doi.org/10.1107/S0021889808042726.
- [36] A.L. Spek, Single-crystal structure validation with the program PLATON, J. Appl. Crystallogr. 36 (2003) 7–13, https://doi.org/10.1107/S0021889802022112.
- [37] P.A. Beckmann, C. Dybowski, A thermometer for nonspinning solid-state NMR spectroscopy, J. Magn. Reson. 146 (2000) 379–380, https://doi.org/10.1006/ jmre.2000.2171.
- [38] A. Bielecki, D.P. Burum, Temperature dependence of ²⁰⁷Pb MAS spectra of solid lead nitrate. an accurate, sensitive thermometer for variable-temperature MAS, J. Magn. Reson., Ser. A 116 (1995) 215–220, https://doi.org/10.1006/ imra.1995.0010.
- [39] N. Brese, M. O'keeffe, Bond-valence parameters for solids, Acta Crystallogr. B Struct. Sci. Cryst. 47 (1991) 192–197, https://doi.org/10.1107/S0108768190011041.
- [40] A. McDermott, F. Creuzet, A. Kolbert, R. Griffin, High-resolution magic-angle-spinning NMR spectra of protons in deuterated solids, J. Magn. Reson. 98 (1992) 408–413, https://doi.org/10.1016/0022-2364(92)90141-S.
- [41] L. Duma, Nitrogen-14 NMR studies of biological systems, eMagRes (2007), https://doi.org/10.1002/9780470034590.emrstm1211.
- [42] S.A. Rouf, V.B. Jakobsen, J. Mareš, N.D. Jensen, C.J. McKenzie, J. Vaara, U.G. Nielsen, Assignment of solid-state ¹³C and ¹H NMR spectra of paramagnetic Ni (II) acetylacetonate complexes aided by first-principles computations, Solid State Nucl. Magn. Reson. 87 (2017) 29–37, https://doi.org/10.1016/ j.ssnmr.2017.07.003.
- [43] A.B. Andersen, A. Pyykkönen, H.J.A. Jensen, V. McKee, J. Vaara, U.G. Nielsen, Remarkable reversal of ¹³C-NMR assignment in d¹, d² compared to d⁸, d⁹ acetylacetonate complexes: analysis and explanation based on solid-state MAS NMR and computations, Phys. Chem. Chem. Phys. 22 (2020) 8048–8059, https:// doi.org/10.1039/D0CP00980F.
- [44] M.C. Tucker, M.M. Doeff, T.J. Richardson, R. Finones, E.J. Cairns, J.A. Reimer, Hyperfine fields at the Li site in LiFePO₄-type olivine materials for lithium rechargeable batteries: a ⁷Li MAS NMR and SQUID study, J. Am. Chem. Soc. 124 (2002) 3832–3833, https://doi.org/10.1021/ja017838m.
- [45] R. Pigliapochi, A.J. Pell, I.D. Seymour, C.P. Grey, D. Ceresoli, M. Kaupp, DFT investigation of the effect of spin-orbit coupling on the NMR shifts in paramagnetic

- solids, Phys. Rev. B 95 (2017), 054412, https://doi.org/10.1103/ PhysRevB.95.054412.
- [46] A.J. Pell, G. Pintacuda, C.P. Grey, Paramagnetic NMR in solution and the solid state, Prog. Nucl. Magn. Reson. Spectrosc. 111 (2019) 1–271, https://doi.org/10.1016/ j.pnmrs.2018.05.001.
- [47] M. Steiner, K. Kakurai, J. Kjems, D. Petitgrand, R. Pynn, Inelastic neutron scattering studies on 1D near-Heisenberg antiferromagnets: a test of the Haldane conjecture, J. Appl. Phys. 61 (1987) 3953–3955, https://doi.org/10.1063/1.338595.
- [48] J. Liu, P.A. Goddard, J. Singleton, J. Brambleby, F. Foronda, J.S. Möller, Y. Kohama, S. Ghannadzadeh, A. Ardavan, S.J. Blundell, T. Lancaster, F. Xiao, R.C. Williams,
- F.L. Pratt, P.J. Baker, K. Wierschem, S.H. Lapidus, K.H. Stone, P.W. Stephens, J. Bendix, T.J. Woods, K.E. Carreiro, H.E. Tran, C.J. Villa, J.L. Manson, Antiferromagnetism in a family of S=1 square lattice coordination polymers NiX₂(pyz)₂ (X=Cl, Br, I, NCS; pyz = pyrazine), Inorg. Chem. 55 (2016) 3515–3529, https://doi.org/10.1021/acs.inorgchem.5b02991.
- [49] A. Meyer, A. Gleizes, J.J. Girerd, M. Verdaguer, O. Kahn, Crystal structures, magnetic anisotropy properties, and orbital interactions in catena-(μ-Nitrito)bis(ethylenediamine)nickel(II) perchlorate and triiodide, Inorg. Chem. 21 (1982) 1729–1739, https://doi.org/10.1021/ic00135a006.